Pd@zeolitic imidazolate framework-8 derived PdZn alloy catalysts for efficient hydrogenation of CO_2 to methanol

Yazhi Yin[1], Bing Hu[1], Xinliang Li, Xiaohai Zhou*, Xinlin Hong*, Guoliang Liu*

College of Chemistry and Molecular Sciences, Wuhan University, Wuhan 430072, PR China

ARTICLE INFO

ABSTRACT

Direct CO_2 hydrogenation to methanol provides a means of CO_2 fixation and a way of hydrogen storage in a more energy-dense and transportable form. Pd-ZnO catalysts can be active for this reaction, but their activities are strongly associated with the preparation methods which influence the dispersion and stability of Pd nanoparticle. Here we report a novel fabrication of highly effective PdZn alloy catalysts derived from Pd@zeolitic imidazolate framework (ZIF-8) for the hydrogenation of CO_2. The confinement of subnanometric Pd particles in the pore framework of ZIF-8 facilitates the formation of Pd-ZnO interfaces with strong-metal-support-interaction (SMSI) after a simple pyrolysis under air condition. The porous texture and high surface area of ZnO ensures a high dispersion of Pd nanoparticles. Different pyrolysis temperatures were studied in catalysis and the highest methanol yield reached $0.65\,\mathrm{g\,g_{cat}^{-1}\,h^{-1}}$ at 270 °C, 4.5 MPa, with a TOF of $972\,\mathrm{h^{-1}}$, over a PdZn catalyst prepared at 400 °C. Such excellent activity has ranked the top reported values over advanced Pd-based catalysts under comparable conditions. The crucial factors for such high methanol yield are the formation of small-sized PdZn alloy particles after H_2 reduction and abundant surface oxygen defects on ZnO. The SMSI between PdZn and ZnO also ensures a long term stability of our PdZn catalysts. At last, we propose the active site that was strongly associated with methanol formation is a PdZn alloy rather than metallic Pd.

1. Introduction

In recent years more and more efforts have been taken to tackle the rising level of CO_2 in the atmosphere by capture, storage and utilization of this earth-abundant carbon source [1,2]. Among them, direct CO_2 hydrogenation to methanol offers a promising means of CO_2 fixation, providing a renewable and sustainable H_2 source is available [3–5]. As "green" hydrogen can be produced from solar energy, biomass and even redundant electric energy [6–8], the methanol synthesis reaction would also be regarded as a way of hydrogen storage in a more energy-dense and transportable form. In the concept of methanol economy for carbon cycle [3], it is very attractive to use renewable methanol as a chemical platform for future fuels and chemical production. Considering catalytic CO_2 conversion to methanol is the crucial initial step, development of efficient catalysts towards methanol production is highly desirable.

Cu-ZnO catalysts have been widely studied towards methanol synthesis [9–11]. The active sites are generally believed to be either CuZn alloy [12] or Cu-ZnO interfaces [13]. Pd has been also reported to be active for CO_2 hydrogenation, but the product selectivity (towards CO or methanol) depends on the type of supports or promoters [9,14].

Use of a proper support such as ZnO and Ga_2O_3 can shift the CO_2 hydrogenation reaction towards methanol synthesis over CO production via the reverse water gas shift reaction (RWGS) [15,16]. Pd-ZnO catalysts, early used in methanol steam reforming reaction [17,18], are studied in the reverse reaction to give methanol with high selectivity. But their performances are strongly associated with the preparation methods which influence the dispersion and stability of Pd or PdZn alloy after reduction [19]. Bahruji et al. recently reported the catalytic activity of Pd-ZnO materials *via* the sol immobilization method showed higher activity than that produced by incipient wetness impregnation because the former possessed PdZn alloy particles with controlled particle size after H_2 treatment [19]. Further, they employed the chemical vapor impregnation method to produce highly dispersed PdZn particles with a mean diameter of 3.9 nm deposited on TiO_2 for efficient methanol production [20]. Our previous work demonstrated Zn enriched small PdZn alloy particles produced by impregnation showed high selectivity towards methanol by suppressing the RWGS reaction [21]. As the dispersion of metal nanoparticles is important for enhancing the number of active sites [22,23], it is believed that maintaining a small particle size of PdZn alloy is crucial to high methanol selectivity

---

* Corresponding authors.
E-mail addresses: zxh7954@whu.edu.cn (X. Zhou), hongxl@whu.edu.cn (X. Hong), liugl@whu.edu.cn (G. Liu).
[1] These authors contributed equally.

and yield.

In recent years, metal organic frameworks (MOFs) have attracted intense attention in catalysis area due to their unique pore/cage properties [24]. Such pore frameworks can effectively confine metal nanoparticles within the pores, especially for noble metals [25]. On the other hand, pyrolysis of a MOF material can give porous metal oxides or even carbon materials, quite dependent on the pyrolysis conditions [26,27]. Inspired by above progresses, we here attempted to prepare Pd-ZnO catalysts, with the two components in close proximity, by using one-pot pyrolysis of Pd incorporated zeolitic imidazolate framework-8 (Pd@ZIF-8) complex. By taking advantage of the confinement effect of the pore framework in ZIF-8, ultrasmall Pd particles were embedded into ZIF-8. Direct calcination of Pd@ZIF-8 under air condition gave desired Pd-ZnO catalysts with controlled Pd particle size ($2 \sim 4$ nm). Different pyrolysis temperatures (350, 400 and 500 °C) were investigated to study their effect on Pd particle size, Pd dispersion and state of surface oxygen. The transformation of Pd to PdZn alloy after reduction by H_2 was also studied by HRTEM, XRD and CO pulse chemisorption. In the subsequent CO_2 hydrogenation reaction, the highest methanol yield was achieved over a PdZn catalyst prepared at 400 °C (PZ8-400). We found that the methanol selectivity and yield were associated to PdZn alloy phase rather than metallic Pd.

2. Experimental section

2.1. Catalyst preparation

$Zn(NO_3)_2 \cdot 6H_2O$ (AR), $Zn(CH_3COO)_2 \cdot 2H_2O$ (AR), NaOH (AR), $NaBH_4$ (AR) and methanol (AR) were purchased from Sinopharm Chemical Reagent Co., Ltd. 2-methylimidazole, Na_2PdCl_4 and ZnO were purchased from Aladdin Co., Ltd. Deionized water was used in all experiments. All chemicals were used as received without further purification.

Synthesis of ZIF-8. ZIF-8 was prepared as reported in the reference [28]. Briefly, 3.7 g $Zn(NO_3)_2 \cdot 6H_2O$ and 1.68 g 2-methylimidazole were dissolved separately in 80 mL methanol. Then, the $Zn(NO_3)_2$ solution was rapidly added into the 2-methylimidazole solution under magnetic stirring at room temperature for 24 h. A white product was collected by centrifugation, rinsed by methanol for four times and then vacuum dried at 50 °C for 12 h.

Synthesis of Pd@ZIF-8. 0.5618 g ZIF-8 was added into a Pd^{2+} solution by dispersing 0.0287 g Na_2PdCl_4 in 10 mL deionized water. After the mixture was under magnetic stirring for 1 h at ambient temperature, 10 ml $NaBH_4$ aqueous solution (1.5 mg mL^{-1}) was quickly added into above solution to reduce Pd^{2+} for 2 h. The obtained Pd@ZIF-8 complex was purified by centrifugation and washed with deionized water and ethanol for three times, followed by a vacuum drying at 50 °C for 12 h. Note that the dosage of Pd was about 5% weight of ZnO derived from ZIF-8 (according to the theoretical formula of ZIF-8, $C_8H_{12}N_4Zn$, 0.2809 g ZIF-8 would convert completely into about 0.1 g ZnO).

Syntheses of the catalysts: PZ8-350, PZ8-400, PZ8-500, PZ(c), PZ(r) and PZ(z). The obtained Pd@ZIF-8 powder was calcined in an air muffle furnace at 350, 400 and 500 °C for 1 h with a heating rate of 2 °C min^{-1}. The products were denoted as PZ8-350, PZ8-400 and PZ8-500 respectively, where P stands for Pd, Z8 for ZIF-8. As a reference, commercial ZnO (20–40 nm), rod-like ZnO and ZIF-8 derived ZnO (ZIF-8-400) were used as the supports for the deposition of Pd via impregnation method, denoted as PZ(c), PZ(r) and PZ(z) respectively, where Z(c), Z(r) and Z(z) stand for commercial ZnO, rod-like ZnO and ZIF-8 derived ZnO. The rod-shaped ZnO nanoparticles were synthesized via a hydrothermal route by Liu's method [29].

2.2. Catalyst characterization

Inductively coupled plasma-atomic emission spectrometry (ICP-AES, IRIS Intrepid II XSP, Thermo Elemental) was used to measure the metal content in the catalysts. To prepare the sample for ICP measurement, 100 mg of catalyst was dissolved in 5 mL of aqua regia and then diluted by 1 vol.% HNO_3 into an aqueous solution of 100 mL. X-ray diffraction (XRD) spectra were recorded on a Bruker D8 Advance X-ray diffractometer with Cu Kα radiation and a generator operating at 40 kV and 40 mA. The samples were scanned from 5° to 85° with a step angle of 0.02°. Thermal gravimetric (TG) measurement was performed on an instrument by TA with a heating rate of 10 °C min^{-1} under air flow. X-ray photoelectron spectra (XPS) were performed on a Thermo Scientific ESCALAB 250Xi X-ray Photoelectron Spectrometer with a monochromatic Al Kα source with an energy of 1486.6 eV and a working power of 150 W (15 kV, 10 mA). The pass energy is 30 eV for core level measurement and 20 eV for valence band measurement. The spot size of the incident X-ray is 500 μm. The emission angle is 0° to the normal. Analyzer resolution is 0.50 eV. Before the test, all samples were pre-reduced in hydrogen at 300 °C for 1 h and then preserved in a container with Fe power inside which can prevent samples from oxidization. Sample data were calibrated by the binding energy of C1s (284.8 eV). The Brunauer-Emmett-Teller (BET) Surface area/porosity measurements were operated on a Micromeritics ASAP-2010 Analyzer with N_2 adsorption-desorption. Transmission electron microscopy (TEM) images were recorded on a JEOL JEM-2010 electron microscope.

CO-pulse chemisorption was conducted on a Micromeritics Autochem 2920. The pretreatment steps are as follows. 0.1 g of the catalyst was placed upon a layer of quartz wool in a U-shaped quartz tube and reduced in a 5%H_2/95%Ar flow of 30 mL min^{-1} at 300 °C for 1 h with a ramping rate of 5 °C min^{-1}. Then Ar (30 mL min^{-1}) was introduced to remove extra hydrogen adsorbed on the surface in the meanwhile cool down the tube to room temperature. Then heating up the sample to 45 °C, the CO-pulse chemisorption was carried out by using 5%CO/95%He. And the signals were detected by a thermal conductivity detector (TCD), using 30 mL min^{-1} of high-purity He as the carrier gas. The adsorption stoichiometry of Pd:CO = 1 was taken as unity [30,31]. H_2 temperature-programmed-reduction (H_2-TPR) measurement of PZ8-400 was carried out from ambient temperature to 300 °C with a heating rate of 5 °C min^{-1} under 5% H_2/Ar atmosphere.
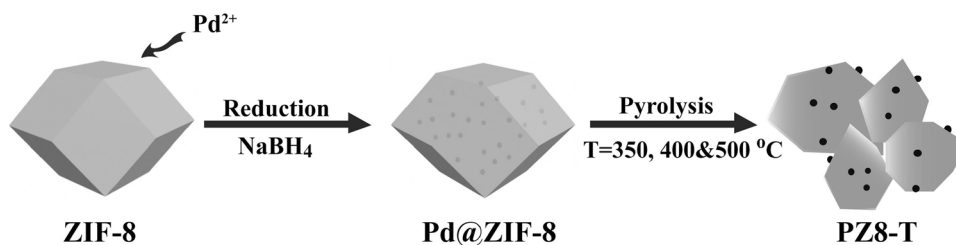
2.3. Catalytic tests

The catalytic tests were carried out on a fixed-bed continue-flow microreactor. Before each test, 0.1 g catalyst was reduced at 300 °C in a flow of pure H_2 (20 ml min^{-1}) for 1 h under atmospheric pressure. After cooling to 80 °C, a CO_2/H_2 mixture with the molar ratio of 1:3 was fed into the reactor and pressurized to 4.5 MPa as controlled by a back-pressure valve. Then the reactant gas flow was set as 36 ml min^{-1} and the reaction temperature was raised up to 250, 270 and 290 °C, respectively. The temperature for the post line of the reactor was maintained at 150 °C to avoid condensation and the effluent products were analyzed online by a gas chromatograph equipped with a TCD detector. The long-term stability was evaluated by a time-on-stream (TOS) test at 270 °C, 4.5 MPa for 50 h.

3. Results and discussion

3.1. Material characterization

The PdZn catalysts were prepared via a direct pyrolysis of Pd@ZIF-8 precursor under air condition, as described in Scheme 1. In the first step, nano-sized ZIF-8 crystals with the particle size of 50–100 nm were prepared following the previous literature [28]. ZIF-8 consists of Zn atoms coordinated with 2-methylimidazole organic framework. The inner cavity diameter of ZIF-8 is about 11.6 Å [32]. Then Pd nanoparticles (NPs) were embedded into the porous ZIF-8 matrix via the reduction of Pd^{2+} with sodium borohydride ($NaBH_4$). Fig. 1 shows the scanning electron microscopy (SEM) and transition electron microscopy (TEM) images of the Pd@ZIF-8 complex. The Pd@ZIF-8 maintains 3D

Scheme 1. The preparation process of the PZ8-T catalysts.

dodecahedron morphologies with diameters in the range of 50–100 nm from SEM analysis (Fig. 1a and b). As for Pd, the TEM image and particle size distribution analysis in Fig. 1c and d reveals the formation of uniform sub-2 nm Pd nanoparticles (1.2 ± 0.2 nm) within the ZIF-8 matrix. It is believed that the pore framework of MOFs can effectively confine the overgrowth of noble metal nanoparticles inside [33,34].

After that, the Pd@ZIF-8 precursor was calcined at different temperatures (350, 400 and 500 °C) under air condition to produce Pd-ZnO, denoted as PZ8-T, where T represents the pyrolysis temperature. ZIF-8 converts into ZnO at a temperature above 350 °C, as confirmed by TGA analysis (Fig. S1). The total weight loss for pure ZIF-8 is 64.2%, consistent with the previous report [35]. XRD analysis in Fig. S2 reveals a complete decomposition of pure ZIF-8 to ZnO after a pyrolysis at 400 °C for 1 h [36]. Interestingly, the doping of Pd impairs the thermal stability of ZIF-8 framework as the collapse temperature of Pd@ZIF-8 shift to around 300 °C, lower than pure ZIF-8 (Fig. S1). Pd facilitates the destruction of the ZIF-8 framework, probably results from a decreased energy for O_2 activation by noble metals [37]. The series of PZ8-T samples were then characterized using XRD and TEM. In Fig. 2a, the crystal form of ZIF-8 was clearly evidenced for the PZ8 sample as a series of diffraction peaks at low angles are assigned to ZIF-8 lattice [32]. When the calcination temperature was set at 350–500 °C, the ZIF-8 phase disappears and converts completely to ZnO as the diffractions

at 31.7°, 34.4°, 36.2°, 47.5°, 66°, and 68° are indexed to wurtzite ZnO (JCPDS#36-1451). Pd species, with a mixed phase of Pd and PdO, were also confirmed from the magnified image (inset in Fig. 2a). But the signals are very weak when compared to those of ZnO, which is probably due to the very low loading of Pd and small sized particles. Fig. 2b–d show the TEM images of PZ8-350, PZ8-400 and PZ8-500, respectively. We can clearly see the presence of Pd NPs supported on ZnO crystals due to their different contrast. The formed ZnO has an average particle size of 20 nm. Such small size of ZnO would benefit the formation of metal-ZnO interfaces for the design of methanol synthesis catalysts with improved activity [12,38]. As for Pd, the average particle size increases to 1.9, 2.9 and 4.2 nm for PZ8-350, PZ8-400 and PZ8-500 when compared to the initial Pd@ZIF-8 precursor (1.2 ± 0.2 nm). The high-temperature treatment, along with the collapse of ZIF-8 network, could inevitably lead to an agglomeration of Pd NPs. In addition, elemental mapping by using high-angle annular dark-field scanning transmission electron microscopy (HAADF-STEM) clearly showed a homogeneous distribution of O, Zn and Pd (Fig. S3). In the final stage, the PZ8-T samples were in-situ reduced under H_2 flow prior to catalytic tests.

Table 1 shows the BET surface area and pore volume data calculated from N_2 sorption isotherms (Fig. S4). ZIF-8 shows the highest surface area (1460 $m^2 g^{-1}$) due to its porous framework. When sub-2 nm Pd
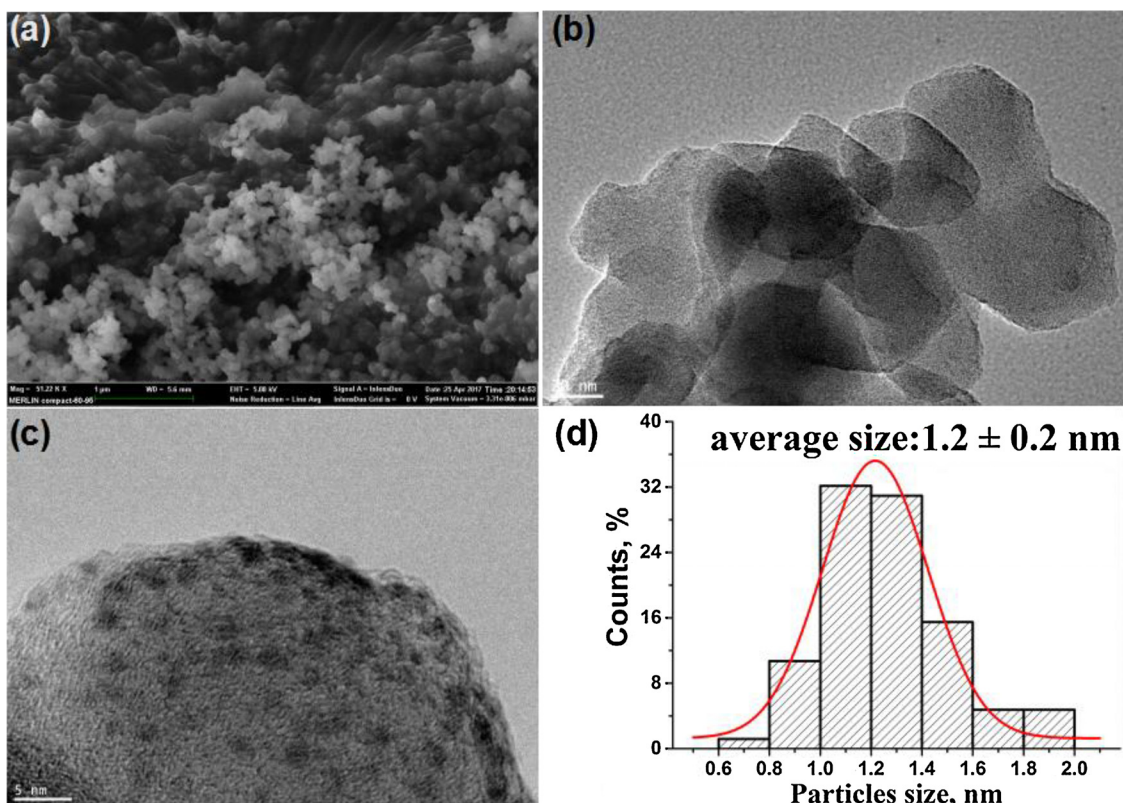

Fig. 1. (a) SEM and (b, c) TEM images and the corresponding (d) histogram of Pd particle size distribution for the Pd@ZIF-8 precursor.
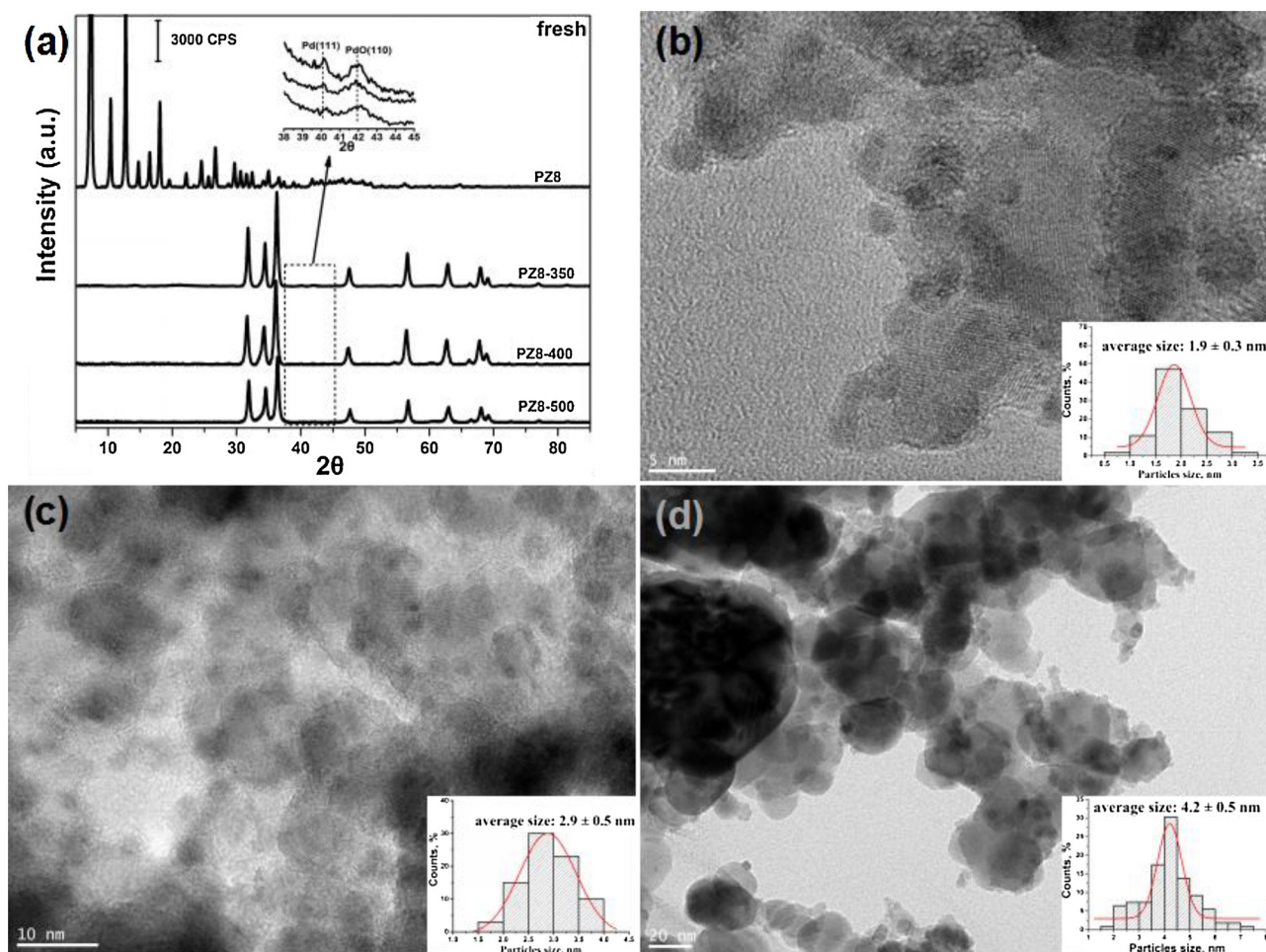
Fig. 2. (a) XRD patterns of fresh PZ8-T samples and referenced PZ8 precursor and (b–d) representative TEM images and the corresponding histograms of Pd particle size distributions for (b) PZ8-350, (c) PZ8-400 and (d) PZ8-500.

Table 1
Physicochemical properties and elemental content data of different samples.

Samples	S_{BET} ($m^2 g^{-1}$)[a]	Pore volume ($cm^3 g^{-1}$)[a]	Metal content (%)[b]	
			Pd	Zn
ZIF-8	1460	0.26	–	–
ZIF-8-400	32	0.21	–	–
PZ8	1281	0.21	2.2	28
PZ8-350	60	0.44	4.1	79
PZ8-400	38	0.26	4.5	72
PZ8-500	17	0.05	4.6	74

[a] S_{BET} and pore volume data are determined by the N_2 sorption isotherms.
[b] Metal contents are detected by ICP-AES.

was embedded into the matrix of ZIF-8, the PZ8 shows a slightly decreased surface area (1281 $m^2 g^{-1}$) and pore volume (0.21 $cm^3 g^{-1}$). After pyrolysis, the surface area is 60, 38 and 17 $m^2 g^{-1}$ for PZ8-350, PZ8-400 and PZ8-500, respectively. A decreasing trend in surface area with the increase in pyrolysis temperature is clearly observed. Note that the PZ8-350 and PZ8-400 samples possess a very high surface area (60 and 38 $m^2 g^{-1}$), which can be comparable to most of the reported advanced value of synthesized ZnO [39,40]. In combination with their large pore volumes, the obtained Pd-ZnO complexes show a porous feature, in agreement with previous reports [36,41]. PZ8-400 shows a higher surface area than ZIF-8-400 (32 $m^2 g^{-1}$), which probably results from the extra surface area contributed by Pd particles. We also measured the Pd content in all pyrolyzed sample by ICP-AES and they show
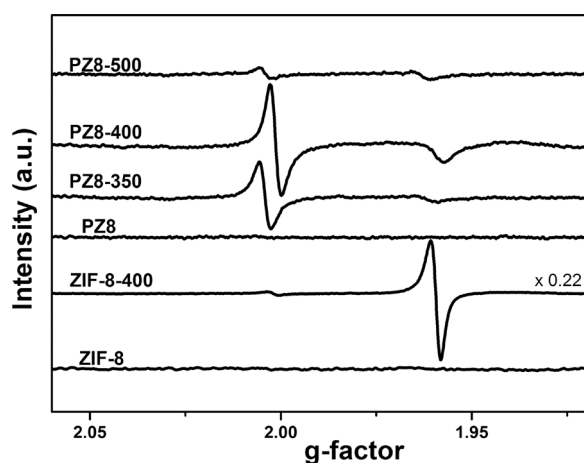

Fig. 3. EPR spectra of different samples.

a very close content of Pd from 4.1 to 4.6% on a weight basis.

Further characterization using electron paramagnetic resonance (EPR) was carried out and the results are shown in Fig. 3. Pure ZIF-8 and Pd@ZIF-8 (PZ8) do not show any electron spin signals. Generally, ZnO shows two characteristic signals at g = 2.00 and g = 1.96 [42]. The former has commonly been assigned to the unpaired electrons deeply trapped in ZnO surface oxygen vacancies, and the signal at g = 1.96 represents unpaired electrons trapped from the CB by shallow

Table 2
Electron spin count numbers per gram of sample calculated from EPR signals.

Samples	Spin count at g = 1.96	Spin count at g = 2.00
ZIF-8	0	0
ZIF-8-400	1.26×10^{10}	7.19×10^{8}
PZ8	0	0
PZ8-350	8.53×10^{8}	2.48×10^{9}
PZ8-400	1.55×10^{9}	3.58×10^{9}
PZ8-500	5.94×10^{8}	2.55×10^{8}

donors (e.g., interstitial Zn) or impurities [42,43]. The ZIF-8 derived pure ZnO (ZIF-8-400) shows a major signal at g = 1.96, while the Pd@ ZIF-8 derived Pd-ZnO sample (PZ8-400) displays a significantly weakened signal at g = 1.96 and an intensified peak at g = 2.00. This indicates that the Pd doping not only facilitates electron transfer from the CB of ZnO to Pd [44] but also promotes the formation of oxygen defects on ZnO surface. The electron transfer supports the presence of strong-metal-support-interactions (SMSI) and would facilitate the formation of oxygen vacancies by shifting the equilibrium ($[O] \leftrightarrow [] + 1/2 O_2 + 2e^-$), which can account for high activity in methanol synthesis from syngas [45,46]. We also quantified the electron spin count of the signal normalized per gram of ZnO at g = 2.00 for different calcined samples (Table 2). The PZ8-400 sample shows the highest spin count (3.58×10^9) when compared with PZ8-350 (2.48×10^9) and PZ8-500 (2.55×10^8), suggesting a high degree of oxygen vacancies on ZnO surface for the PZ8-400 sample. It can be concluded that direct pyrolysis of the Pd@ZIF-8 precursor under air condition facilitates the formation of Pd-ZnO interfaces with SMSI as well as abundant surface oxygen vacancies on ZnO.

3.2. Evidence for PdZn alloy formation after H2 reduction

A reduced state of Pd based catalysts is essential to the CO_2 hydrogenation reaction. All catalysts were reduced by pure H_2 and their phase composition and microstructures were further examined using XRD and TEM. Fig. 4a shows the XRD patterns of reduced PZ8-T and PZ8 samples. The main phase of ZnO or ZIF-8 phase is almost remained after H_2 treatment (compared with Fig. 2a).Fig. 4b shows the magnified region for analysis of Pd crystal phase. The diffraction peaks for metallic Pd and PdO disappear. Instead, there emerge two new peaks at $2\theta = 41.2°$ and $44.1°$, which are assigned to the (111) and (200) diffractions of PdZn alloy (Pd_1Zn_1, PDF #06-0620).This indicates that Pd and PdO convert into PdZn alloy phase with neighboring ZnO after H_2 reduction. The formation of PdZn alloy can be further confirmed by high-resolution TEM analysis. As seen in Fig. 5, a lattice spacing of

0.219 nm is assigned to the characteristic (111) facet of PdZn alloy for three reduced PZ8-T samples. Through measuring the fringes in different area, PdZn (111) lattice fringes can be easily found, while pure Pd lattice with a (111) d-spacing of 0.230 nm is very rare. As the accuracy of measurement is only 0.005 nm, we believe it is reasonable to distinguish the lattice of Pd and PdZn. It is reported that Pd has a high tendency to alloy with Zn under H_2 treatment and the formed PdZn alloy is responsible for methanol steam reforming and reverse CO_2 hydrogenation reaction [19,47]. We then acquired the Pd particle size distributions from TEM analysis for three reduced catalysts. As shown in Fig. 5, the average Pd particle size is measured to be 4.3, 3.7 and 5.8 nm for reduced PZ8-350, PZ8-400 and PZ8-500, respectively. It is found that the Pd particle size increases when compared to those of fresh samples (1.9, 2.9 and 4.2 nm in Fig. 2). This is due to the formation of PdZn alloy, which agrees with previous reports [48]. During the H_2 treatment, with the assistance of hydrogen spillover effect from Pd, Zn atoms from neighboring ZnO diffuse to Pd surface and intermix with Pd atoms to form a bilayer or even thick PdZn alloy film [49,50]. With time going, bulk PdZn phase would be formed.

From the previous reports, the formation of PdZn alloy phase takes place at above 180 °C under H_2 flow [19,51]. This can be confirmed by our H_2 TPR profile where a broad H_2 consumption peak for PdZn alloy starts from ∼180 °C (Fig. S5). At around 120 °C, Pd is mainly in the phase of monometallic Pd. To study the evolution of PdZn alloy, we chose 120 and 300 °C as the pre-reduction temperatures for the PZ8-T samples prior to CO pulse chemisorption measurements. The number of surface Pd atoms and the Pd dispersion were calculated based on the amount of CO consumption with an assumption of Pd/CO = 1 (see calibration in Fig. S6) and the results are listed in Table 3. For all tested samples, the treatment at 300 °C leads to a significant decrease in the number of exposed Pd atoms and the corresponding Pd dispersion by 44–54%, indicative of the formation of PdZn alloy. During the conversion of Pd to PdZn alloy, a replacement of surface Pd by Zn atoms takes place. The previous literature has shown that alloying Pd could greatly decrease the number of exposed Pd [52–54]. This can probably explain the gradual increase in Pd particle size after alloying as well. By comparing different PZ8-T samples reduced at 300 °C, PZ8-400 shows the highest number of exposed Pd ($21.55\,\mu mol\,g^{-1}$) and the highest dispersion (5.1%). This is consistent with the fact that PZ8-400 possesses the smallest Pd particle size among three reduced samples (Fig. 5 and Table 3). This suggests that a moderate calcination temperature is necessary for the maximum exposure of surface Pd. Note that the dispersion of PZ8-500 is much lower than that of PZ8-400 and PZ8-350 under both treatment conditions due to the sintering of Pd at high pyrolysis temperature, which can be confirmed by the increased Pd particle size from TEM analysis (Fig. 5 and Table 3).
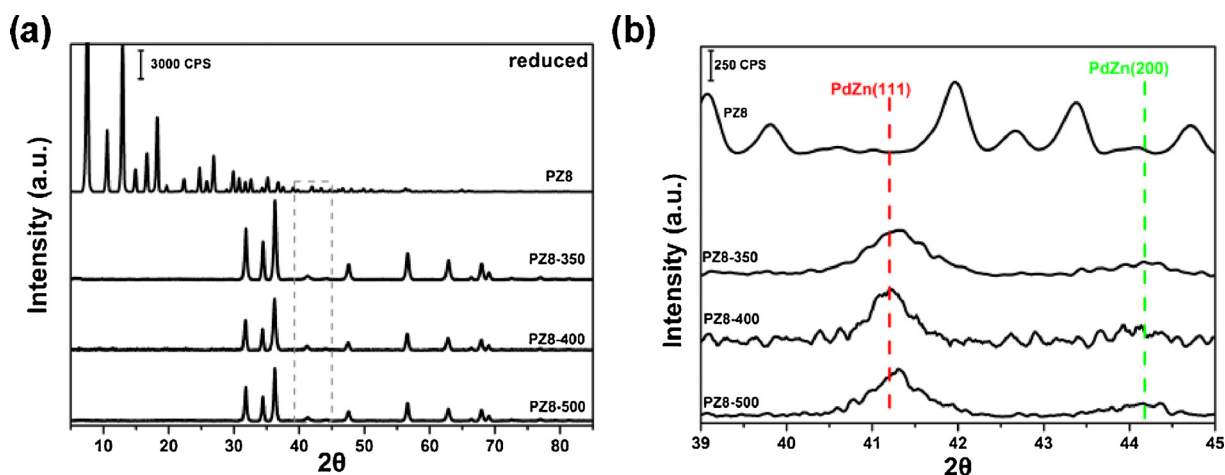

Fig. 4. (a) XRD patterns of different catalysts after H_2 reduction and (b) the magnified region for analysis of Pd crystal phase.
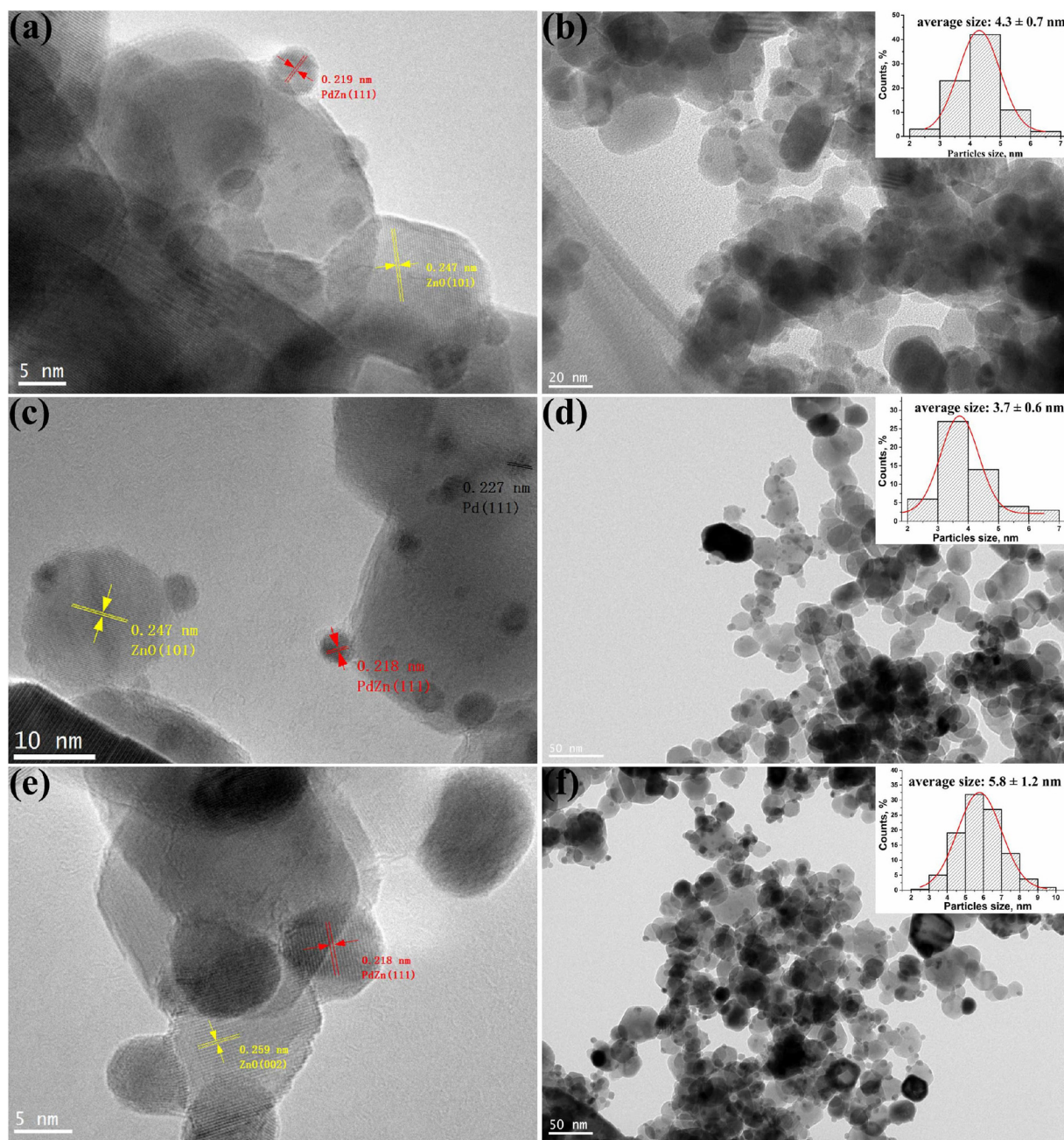
Fig. 5. Representative HRTEM and TEM images and the corresponding histograms of Pd particle size distributions for reduced (a, b) PZ8-350, (c, d) PZ8-400 and (e, f) PZ8-500 after H_2 treatment.

Table 3
Effect of different treatments on the exposed Pd atoms (Pd_S), Pd dispersion and Pd particle size for different PZ8-T samples.

Samples	120 °C		300 °C		D_{Pd} (nm)[c]	D_{PdZn} (nm)[d]
	Pd_S (µmol g^{-1})[a]	Pd dispersion (%)[b]	Pd_S (µmol g^{-1})[a]	Pd dispersion (%)[b]		
PZ8-350	37.07	9.6	17.06	4.4	1.9	4.3
PZ8-400	38.23	9.0	21.55	5.1	2.9	3.7
PZ8-500	20.61	4.8	9.40	2.2	4.2	5.8

[a] Pd_S is determined by CO pulse chemisorption based on an assumption of Pd/CO = 1 [30,31].
[b] Pd dispersion = exposed Pd atoms/total Pd atoms.
[c] D_{Pd} stands for the average Pd particle size in fresh catalysts.
[d] D_{PdZn} stands for the average PdZn particle size in reduced catalysts.
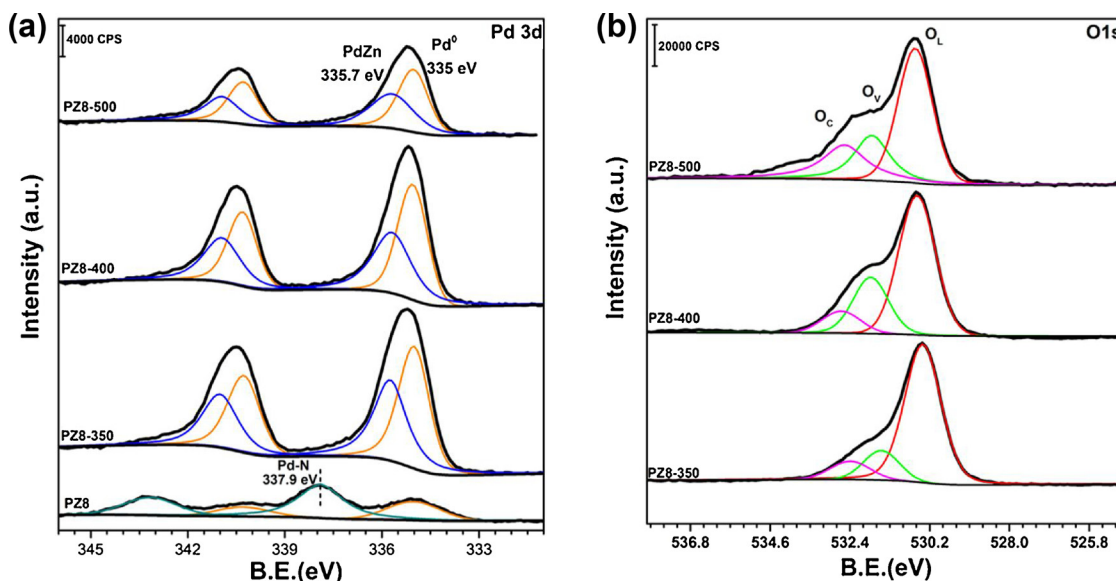
Fig. 6. Deconvolution of (a) Pd 3d and (b) O 1s XPS spectra for different reduced catalysts.

We next performed XPS characterization to acquire information about the chemical state of Pd and O for all reduced samples (see survey spectra in Fig. S7). Fig. 6a displays Pd 3d core level XPS spectra. After deconvolution, we can see two types of Pd species for the PZ8-T samples: 335.0 eV for metallic Pd and 335.7 eV for PdZn [55]. It has been reported alloying Pd with Zn leads to a chemical shift to higher binding energy by 0.6–1 eV due to electron modifications [47,56]. The PdZn alloy accounts for 46%, 46% and 45% of total surface Pd atoms for PZ8-350, PZ8-400 and PZ8-500, respectively (Table S1). XPS valance band spectra also confirmed the presence of metallic Pd, PdZn alloy and ZnO phase (see detailed discussion in Fig. S8 in SI). By contrast, the PZ8 sample contains two types of Pd species: metallic Pd and highly oxidized Pd with a binding energy at 337.9 eV. The extraordinary high-valence of Pd is probably caused by partial ionization of surface Pd when coordinated by 2-methylimidazole via Pd 4d/N 2p charge transfer and Pd (4d)/Pd (5s,5p) rehybridization [57], suggesting the strong interactions between Pd NPs and ZIF-8 backbones. The high-valence Pd entity accounts for 68% of total surface Pd in PZ8 (Table S1). Fig. 6b shows the deconvolution of O 1s XPS spectra for all PZ8-T samples. The main peak at around 530.5 eV (O_L) is assigned to the lattice oxygen of ZnO for three PZ8-T samples. The medium binding energy at 531.8 eV (O_V) is attributed to O^{2-} in the oxygen deficient regions within the ZnO matrix. The O_C peak at 532.5 eV is usually assigned to chemisorbed and dissociated O species or OH [58,59]. From Table S2, the increase in the total content of O_V and O_C can somehow reflect the increased degree of surface disorder (defects) with the increase in the pyrolysis temperature. As for the Zn 2p XPS spectra in Fig. S9, it is almost impossible to distinguish between PdZn and ZnO due to the very low content of Zn in PdZn phase.

3.3. Catalytic performance

We next investigated the activity of different catalysts in CO_2 hydrogenation reaction at 250–290 °C and at 4.5 MPa pressure. The catalytic results are shown in Fig. 7. All PZ8-T samples show much higher activity than the referenced PZ8 sample at the whole range of reaction temperature, in terms of CO_2 conversion and methanol selectivity. For the three PZ8-T samples, the order for CO_2 conversion is PZ8-500 > PZ8-400 > PZ8-350 (Fig. 7a), but the order for methanol selectivity shows the opposite trend (Fig. 7b). The methanol selectivity decreases with the increase in reaction temperature, well consistent with the exothermic nature of methanol synthesis reaction

(-49.5 kJ mol^{-1} at 298 K) when compared to the generation of CO via the endothermic reverse water gas shift (RWGS) reaction (41.2 kJ mol^{-1} at 298 K) [60]. By contrast, the PZ8 catalyst disfavors the methanol production with a selectivity of only 13% at 250 °C. The major product is CO (87% selectivity, Fig. 7c) as no clear PdZn alloy is formed (Figs. 4 and 6). Very unusually, when the reaction temperature is further increased to 290 °C, the methanol selectivity quickly goes up and reaches around 40%, which is comparable to that of PZ8-500. Such significant change implies an in situ formation of active sites for methanol synthesis during reaction. It is speculated that the gradual formation of ZnO from the decomposition of ZIF-8 and then the in situ evolution of PdZn alloy sites may take place under such a harsh condition (250–290 °C and 4.5 MPa of mixed H_2/CO_2). The presence of newly formed ZnO and PdZn was then evidenced from the XRD pattern of used PZ8 catalyst (Fig. S10). A similar phenomenon for an un-reduced Pd-ZnO catalyst was reported by Bahruji et al., as they found the formation of PdZn phase takes place in situ during the reaction [19].

The methanol STY gives an integrated evaluation of a catalyst. As shown in Fig. 7d, all the PZ8-T catalysts give a peak of methanol STY at 270 °C, as the methanol production is overwhelmed by CO formation to a greater extent at a higher temperature. Among them, PZ8-400 shows the highest methanol STY (0.65 g g_{cat}^{-1} h^{-1}), slightly greater than that over PZ8-350 (0.62 g g_{cat}^{-1} h^{-1}) and PZ8-500 (0.62 g g_{cat}^{-1} h^{-1}). In comparison, the methanol STY over the PZ8 catalyst increases quickly with the increase in reaction temperature due to the in situ formation of PdZn alloy phase, but it is still far away from that over the calcined catalysts. Note that the activity of PZ8-400 in terms of methanol yield per gram of active metal (Pd in this work) reaches 11.3 and 14.4 $g_{methanol}$ g_{Pd}^{-1} h^{-1} at 250 and 270 °C, respectively. With the surface area of Pd taken into account (active sites per gram of catalyst), the methanol TOF of the PZ8-400 catalyst reaches 972 h^{-1} at 270 °C and 4.5 MPa. Such excellent activity motivated us to perform the reaction under low pressure, for example, 2 MPa. Low-pressure methanol synthesis has great potential to couple with low pressure CO_2/H_2 mixture feeds produced from low temperature aqueous phase reforming (APR) of biomass derivatives [21]. The catalytic tests under 250 °C, 2 MPa show the conversion of CO_2 and selectivity to methanol reaches 6.2% and 47%, respectively (Table S3). The methanol selectivity is lower than that under 4.5 MPa (63%) due to the fact that high pressure favors the methanol synthesis reaction ($CO_2 + 3H_2 \rightarrow CH_3OH + H_2O$) according to the classical Le Chatelier's principle [61]. Regarding the methanol yield per gram of catalyst, the reaction rate reaches 0.22
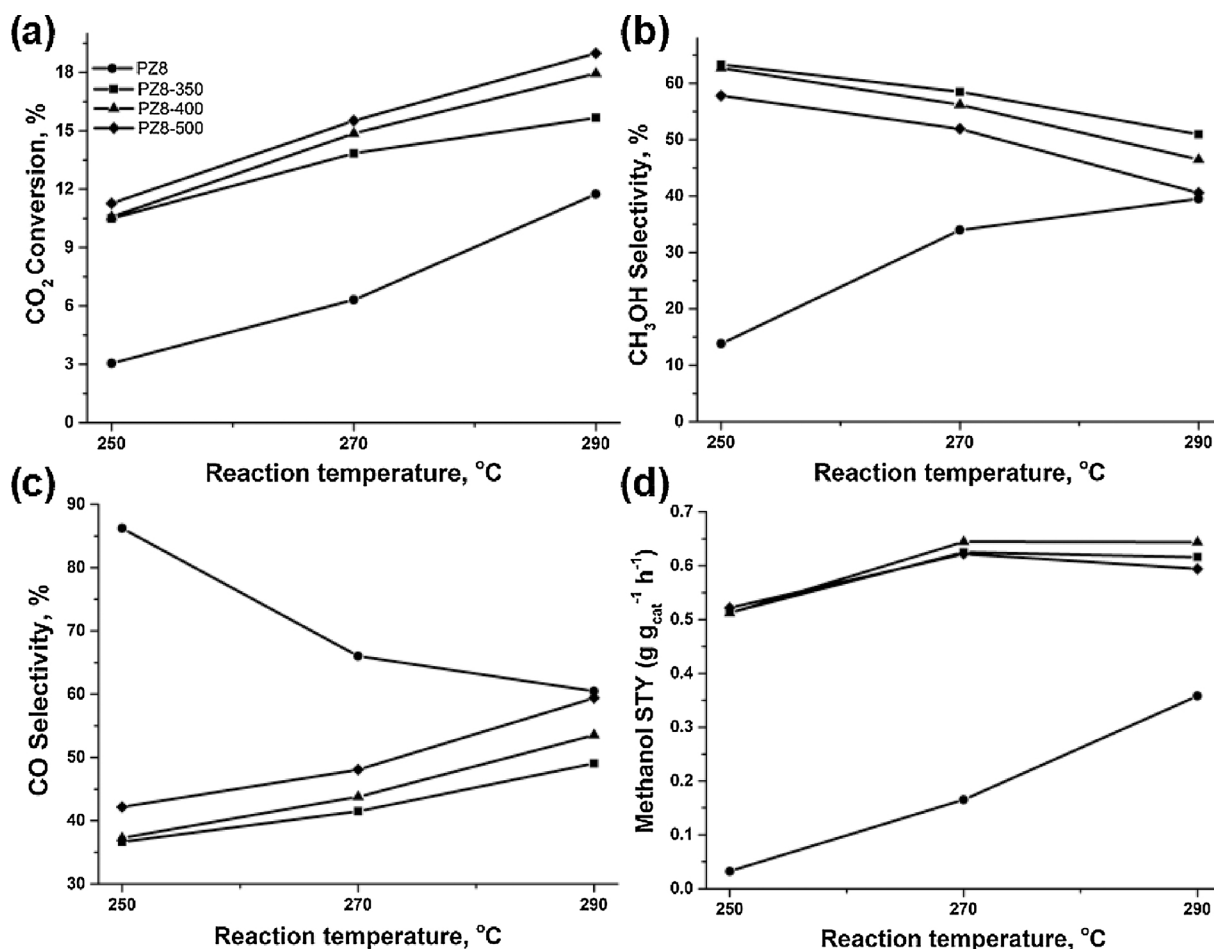
Fig. 7. Catalytic performance of different catalysts, in terms of (a) CO_2 conversion, (b) methanol selectivity, (c) CO selectivity and (d) methanol STY.

$g_{methanol}\,g_{cat}^{-1}\,h^{-1}$ for CO_2 hydrogenation at 2 MPa (Table S3). To our best knowledge, the activity of PZ8-400 is higher than most of the ever-reported advanced Pd based catalysts under comparable reaction conditions (see Table S3).

The activity of PZ8-400 catalyst was then compared with other PdZn catalysts synthesized via the post-deposition method. Different types of ZnO substrates including ZnO rods, ZIF-8 derived porous ZnO and commercial ZnO powder were investigated (see details in the experimental section). All catalysts show comparable BET surface area and ZnO particle size (Table S4), ruling out the interference by ZnO surface. Clearly, the PZ8-400 sample shows the highest methanol selectivity (56.2%) as well as the highest methanol STY ($0.65\,g\,g_{cat}^{-1}\,h^{-1}$) when compared to the PZ (c) (48.3%, $0.60\,g\,g_{cat}^{-1}\,h^{-1}$), PZ (z) (46.2%, $0.56\,g\,g_{cat}^{-1}\,h^{-1}$) and PZ (r) (40.9%, $0.46\,g\,g_{cat}^{-1}\,h^{-1}$). As the methanol production is associated with PdZn alloy phase at Pd-ZnO interface, we believe the encapsulation structure of Pd@ZIF-8 favors the interactions between Pd and ZnO upon one-pot pyrolysis, and thus facilitates the formation of PdZn alloy phase when treated by H_2 reduction.

We next performed a time-on-stream (TOS) test to examine the long-term durability of the PZ8-400 catalyst. Fig. 8 shows catalytic results including CO_2 conversion, methanol selectivity and methanol yield at 270 °C, 4.5 MPa for 50 h. The CO_2 conversion slightly decreases from initial 15.1% to 13.6% while the methanol selectivity increases gradually from 51.9% to 54.2% after 50 h. As a result, the final methanol STY marginally drops by only 6% with reference to the initial yield. After the TOS test, the PZ8-400 catalyst was cooled down under H_2 atmosphere and then carefully collected for further characterization. TEM images in Fig. S11 indicated that the structures were retained and
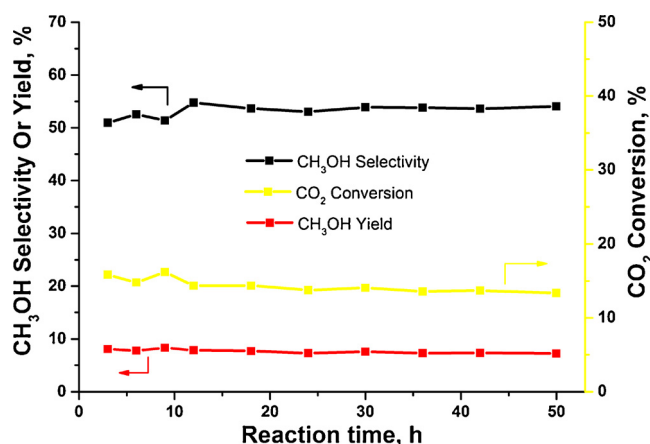

Fig. 8. Time-on-stream test of the PZ8-400 catalyst in CO_2 hydrogenation to methanol at 270 °C for 50 h. Reaction conditions: pressure = 4.5 MPa, H_2/CO_2 = 3:1, gas flow = 36 mL min^{-1}, catalyst mass = 0.1 g (GHSV = 21,600).

the average Pd particle size gradually increased to 5.1 nm, slightly larger than that of reduced sample (3.7 nm). The crystal phase remained unchanged from XRD pattern of spent PZ8-400 catalyst (Fig. S12). All above analyses confirm the stability of the PZ8-400 catalyst for CO_2 hydrogenation to methanol.

3.4. Discussion on active sites for methanol synthesis

It is generally believed that the activities of Pd based catalysts for

methanol synthesis reaction are much dependent on the choice of supports [14]. Monometallic Pd is only active for CO production *via* the RWGS reaction, as confirmed by the performance of Pd@ZIF-8. Alloying Pd with Zn or Ga favors the methanol formation reaction [15,16], probably results from the modulation of the electronic structure of Pd. Previous literature has shown that alloying leads to charge transfer to fill the d-band of Pd and thus shift it below the Fermi level, with a behavior being more like Cu. Pd can easily dissociate H_2, but has poor adsorption towards CO_2 [62]. By contrast, Zn doped Pd surface (e.g., Pd_1Zn_1 alloy) would decrease the capability of H_2 dissociation to some extent but enhance the adsorption of CO_2 instead. A moderate adsorption (neither too strong nor too weak) is necessary for a reaction to happen, according to the Sabatier principle. Our previous DFT calculations have shown that the pure Pd (111) surface favors the formation of COOH* over HCOO* intermediates after initial hydrogenation step [21]. The former tends to decompose to CO with a low activation barrier while the HCOO* species, as the pivotal intermediates for methanol synthesis, are not stable on pure Pd surface and so will decompose there, rather than make methanol. In contrast, HCOO* is much more favoured and stabilized on Pd_1Zn_1 surface. Zn decoration onto Pd surface could also benefit the adsorption of further hydrogenated O-anchored species such as HCOOH*, H_2CO* and CH_3OH* since Zn has strong affinity to oxygen [13]. The selective formation of HCOO* over COOH* on PdZn alloy leads to enhanced methanol selectivity through further multi-step hydrogenation. This can explain the high selectivity of our PZ8-T catalysts as well as the gradual increase in methanol selectivity with the increase in reaction temperature over Pd@ZIF-8 catalyst due to the in situ evolution of PdZn alloy phase.

It is also reported that CO_2 can easily adsorb on ZnO or Ga_2O_3 to form carbonate-like surface complexes during the hydrogenation reaction [63–65]. Our earlier studies have shown that modifying the shape and surface properties of ZnO and Ga_2O_3 can improve the catalytic performance of Cu or Pd catalysts [44,66]. Surface oxygen vacancies on ZnO strengthen the CO_2 interaction by increasing the electron transfer to CO_2 from the polarons and thus facilitate the chemisorption of CO_2 [67]. Our PZ8-400 catalyst possesses a high content of surface oxygen defects, as evidenced from the above EPR and XPS analyses. This is probably another reason to explain the excellent activity of PZ8-400.

4. Conclusions

We have reported a novel method to synthesize PdZn alloy catalysts derived from the Pd@ZIF-8 precursor for efficient hydrogenation of CO_2 to methanol. The pore framework of ZIF-8 was used to confine the growth of Pd particles to subnano-level. Direct pyrolysis of the Pd@ZIF-8 precursor under air condition facilitated the formation of Pd-ZnO interfaces. The porous texture and high surface area of ZnO ensures a high dispersion of Pd nanoparticles, and in turn, the Pd incorporation accelerates the decomposition of ZIF-8 to ZnO with a large number of surface oxygen defects. Upon pre-reduction by H_2, metallic Pd would transform into PdZn alloy phase, verified by HRTEM and XRD. CO pulse chemisorption was also used to quantify the amount of surface Pd atoms which showed that nearly half of the surface Pd atoms were replaced by Zn atoms after the formation of PdZn alloy. The highest methanol yield reached $0.65\,g\,g_{cat}^{-1}\,h^{-1}$, with a TOF of $972\,h^{-1}$, at 270 °C, 4.5 MPa over a PZ8-400 catalyst. Such excellent activity probably resulted from numerous small-sized PdZn alloy particles and high content of oxygen defects on ZnO surface. Strong interactions between Pd and ZnO support also ensured a long term stability of our PdZn catalysts. At last, we believe a PdZn alloy rather than metallic Pd is the true active site for methanol formation. Hopefully, this work provides a new route for the preparation of efficient PdZn catalysts with controlled particle size and provides knowledge on the understanding of the active sites for methanol synthesis reaction.

Appendix A. Supplementary data

Supplementary material related to this article can be found, in the online version, at doi:https://doi.org/10.1016/j.apcatb.2018.04.024.

References

[1] M.E. Boot-Handford, J.C. Abanades, E.J. Anthony, M.J. Blunt, S. Brandani, N. Mac Dowell, J.R. Fernandez, M.C. Ferrari, R. Gross, J.P. Hallett, R.S. Haszeldine, P. Heptonstall, A. Lyngfelt, Z. Makuch, E. Mangano, R.T.J. Porter, M. Pourkashanian, G.T. Rochelle, N. Shah, J.G. Yao, P.S. Fennell, Carbon capture and storage update, Energy Environ. Sci. 7 (2014) 130–189.

[2] C.A. Trickett, A. Helal, B.A. Al-Maythalony, Z.H. Yamani, K.E. Cordova, O.M. Yaghi, The chemistry of metal-organic frameworks for CO2 capture, regeneration and conversion, Nat. Rev. Mater. 2 (2017), http://dx.doi.org/10.1038/natrevmats. 2017.45.

[3] G.A. Olah, Beyond oil and gas: the methanol economy, Angew. Chem. Int. Ed. 44 (2005) 2636–2639.

[4] W. Wang, S. Wang, X. Ma, J. Gong, Recent advances in catalytic hydrogenation of carbon dioxide, Chem. Soc. Rev. 40 (2011) 3703–3727.

[5] J. Ma, N. Sun, X. Zhang, N. Zhao, F. Mao, W. Wei, Y. Sun, A short review of catalysis for CO_2 conversion, Catal. Today 148 (2009) 221–231.

[6] J.A. Turner, Sustainable hydrogen production, Science 305 (2004) 972–974.

[7] X. Wang, K. Maeda, A. Thomas, K. Takanabe, G. Xin, J.M. Carlsson, K. Domen, M. Antonietti, A metal-free polymeric photocatalyst for hydrogen production from water under visible light, Nat. Mater. 8 (2009) 76–80.

[8] I.K. Kapdan, F. Kargi, Bio-hydrogen production from waste materials, Enzyme Microb. Technol. 38 (2006) 569–582.

[9] S.G. Jadhav, P.D. Vaidya, B.M. Bhanage, J.B. Joshi, Catalytic carbon dioxide hydrogenation to methanol: a review of recent studies, Chem. Eng. Res. Des. 92 (2014) 2557–2567.

[10] M.M. Günter, T. Ressler, B. Bems, C. Büscher, T. Genger, O. Hinrichsen, M. Muhler, R. Schlögl, Implication of the microstructure of binary Cu/ZnO catalysts for their catalytic activity in methanol synthesis, Catal. Lett. 71 (2001) 37–44.

[11] Q. Sun, Y.L. Zhang, H.Y. Chen, J.F. Deng, D. Wu, S.Y. Chen, Novel process for the preparation of Cu/ZnO and Cu/ZnO/Al2O3 ultrafine catalyst: structure, surface properties, and activity for methanol synthesis from $CO_2 + H_2$, J. Catal. 167 (1997) 92–105.

[12] M. Behrens, F. Studt, I. Kasatkin, S. Kühl, M. Hävecker, F. Abild-Pedersen, S. Zander, F. Girgsdies, P. Kurr, B.L. Kniep, M. Tovar, The active site of methanol synthesis over Cu/ZnO/Al2O3 industrial catalysts, Science 336 (2012) 893–897.

[13] S. Kattel, P.J. Ramirez, J.G. Chen, J.A. Rodriguez, P. Liu, Active sites for CO_2 hydrogenation to methanol on Cu/ZnO catalysts, Science 355 (2017) 1296–1299.

[14] A. Erdöhelyi, M. Pásztor, F. Solymosi, Catalytic hydrogenation of CO_2 over supported palladium, J. Catal. 98 (1986) 166–177.

[15] X.-L. Liang, X. Dong, G.-D. Lin, H.-B. Zhang, Carbon nanotube-supported Pd-ZnO catalyst for hydrogenation of CO_2 to methanol, Appl. Catal. B-Environ. 88 (2009) 315–322.

[16] T. Fujitani, M. Saito, Y. Kanai, T. Watanabe, J. Nakamura, T. Uchijima, Development of an active Ga2O3 supported palladium catalyst for the synthesis of methanol from carbon dioxide and hydrogen, Appl. Catal. A: Gen. 125 (1995) L199–L202.

[17] N. Iwasa, S. Masuda, N. Ogawa, N. Takezawa, Steam reforming of methanol over Pd/ZnO: effect of the formation of PdZn alloys upon the reaction, Appl. Catal. A: Gen. 125 (1995) 145–157.

[18] S. Sá, H. Silva, L. Brandão, J.M. Sousa, A. Mendes, Catalysts for methanol steam reforming-a review, Appl. Catal. B-Environ. 99 (2010) 43–57.

[19] H. Bahruji, M. Bowker, G. Hutchings, N. Dimitratos, P. Wells, E. Gibson, W. Jones, C. Brookes, D. Morgan, G. Lalev, Pd/ZnO catalysts for direct CO_2 hydrogenation to methanol, J. Catal. 343 (2016) 133–146.

[20] H. Bahruji, M. Bowker, W. Jones, J. Hayward, J.R. Esquius, D.J. Morgan, G.J. Hutchings, PdZn catalysts for CO_2 hydrogenation to methanol using chemical vapour impregnation (CVI), Faraday Discuss. 197 (2017) 309–324.

[21] F. Liao, X.-P. Wu, J. Zheng, M.M.-J. Li, A. Kroner, Z. Zeng, X. Hong, Y. Yuan, X.-Q. Gong, S.C.E. Tsang, A promising low pressure methanol synthesis route from CO_2 hydrogenation over Pd@Zn core-shell catalysts, Green Chem. 19 (2017) 270–280.

[22] D.K. Liguras, D.I. Kondarides, X.E. Verykios, Production of hydrogen for fuel cells by steam reforming of ethanol over supported noble metal catalysts, Appl. Catal. B-Environ. 43 (2003) 345–354.

[23] S.J. Tauster, S.C. Fung, R.L. Garten, Strong metal-support interactions. Group 8 noble metals supported on titanium dioxide, J. Am. Chem. Soc. 100 (1978) 170–175.

[24] J.Y. Lee, O.K. Farha, J. Roberts, K.A. Scheidt, S.T. Nguyen, J.T. Hupp, Metal-organic framework materials as catalysts, Chem. Soc. Rev. 38 (2009) 1450–1459.

[25] S. Hermes, M.K. Schröter, R. Schmid, L. Khodeir, M. Muhler, A. Tissler, R.W. Fischer, R.A. Fischer, Metal@ MOF: loading of highly porous coordination

polymers host lattices by metal organic chemical vapor deposition, Angew. Chem. Int. Ed. 44 (2005) 6237–6241.

[26] W.-T. Koo, S.-J. Choi, S.-J. Kim, J.-S. Jang, H.L. Tuller, I.-D. Kim, Heterogeneous sensitization of metal-organic framework driven metal@metal oxide complex catalysts on an oxide nanofiber scaffold toward superior gas sensors, J. Am. Chem. Soc. 138 (2016) 13431–13437.

[27] H.-L. Jiang, B. Liu, Y.-Q. Lan, K. Kuratani, T. Akita, H. Shioyama, F. Zong, Q. Xu, From metal-organic framework to nanoporous carbon: toward a very high surface area and hydrogen uptake, J. Am. Chem. Soc. 133 (2011) 11854–11857.

[28] S. Liu, J. Wang, J. Yu, ZIF-8 derived bimodal carbon modified ZnO photocatalysts with enhanced photocatalytic CO₂ reduction performance, RSC Adv. 6 (2016) 59998–60006.

[29] B. Liu, H.C. Zeng, Room temperature solution synthesis of monodispersed single-crystalline ZnO nanorods and derived hierarchical nanostructures, Langmuir 20 (2004) 4196–4204.

[30] I. Simakova, O. Simakova, P. Maki-Arvela, A. Simakov, M. Estrada, D.Y. Murzin, Deoxygenation of palmitic and stearic acid over supported Pd catalysts: effect of metal dispersion, Appl. Catal. A-Gen. 355 (2009) 100–108.

[31] R. Strobel, F. Krumeich, W.J. Stark, S.E. Pratsinis, A. Baiker, Flame spray synthesis of Pd/Al₂O₃ catalysts and their behavior in enantioselective hydrogenation, J. Catal. 222 (2004) 307–314.

[32] K.S. Park, Z. Ni, A.P. Côté, J.Y. Choi, R. Huang, F.J. Uribe-Romo, H.K. Chae, M. O'Keeffe, O.M. Yaghi, Exceptional chemical and thermal stability of zeolitic imidazolate frameworks, Proc. Natl. Acad. Sci. U. S. A. 103 (2006) 10186–10191.

[33] Q. Yang, Q. Xu, H.-L. Jiang, Metal-organic frameworks meet metal nanoparticles: synergistic effect for enhanced catalysis, Chem. Soc. Rev. 46 (2017) 4774–4808.

[34] P. Valvekens, F. Vermoortele, D. De Vos, Metal-organic frameworks as catalysts: the role of metal active sites, Catal. Sci. Technol. 3 (2013) 1435–1445.

[35] K. Kida, M. Okita, K. Fujita, S. Tanaka, Y. Miyake, Formation of high crystalline ZIF-8 in an aqueous solution, CrystEngComm 15 (2013) 1794–1801.

[36] Y. Pan, Y. Liu, G. Zeng, L. Zhao, Z. Lai, Rapid synthesis of zeolitic imidazolate framework-8 (ZIF-8) nanocrystals in an aqueous system, Chem. Commun. 47 (2011) 2071–2073.

[37] M. Fernández-García, A. Martínez-Arias, L.N. Salamanca, J.M. Coronado, J.A. Anderson, J.C. Conesa, J. Soria, Influence of ceria on Pd activity for the CO + O₂ reaction, J. Catal. 187 (1999) 474–485.

[38] S. Kuld, M. Thorhauge, H. Falsig, C.F. Elkjaer, S. Helveg, I. Chorkendorff, J. Sehested, Quantifying the promotion of Cu catalysts by ZnO for methanol synthesis, Science 352 (2016) 969–974.

[39] S. Kaluza, M.K. Schroeter, R.N. d'Alnoncourt, T. Reinecke, M. Muhler, High surface area ZnO nanoparticles via a novel continuous precipitation route, Adv. Funct. Mater. 18 (2008) 3670–3677.

[40] Q. Zhang, T.R. Chou, B. Russo, S.A. Jenekhe, G. Cao, Aggregation of ZnO nano-crystallites for high conversion efficiency in dye-sensitized solar cells, Angew. Chem. Int. Ed. 47 (2008) 2402–2406.

[41] Y. Du, R.Z. Chen, J.F. Yao, H.T. Wang, Facile fabrication of porous ZnO by thermal treatment of zeolitic imidazolate framework-8 and its photocatalytic activity, J. Alloy Compd. 551 (2013) 125–130.

[42] V. Ischenko, S. Polarz, D. Grote, V. Stavarache, K. Fink, M. Driess, Zinc oxide nanoparticles with defects, Adv. Funct. Mater. 15 (2005) 1945–1954.

[43] C.G. Van de Walle, Defect analysis and engineering in ZnO, Phys. B 308 (2001) 899–903.

[44] F. Liao, Y. Huang, J. Ge, W. Zheng, K. Tedsree, P. Collier, X. Hong, S.C. Tsang, Morphology-dependent interactions of ZnO with Cu nanoparticles at the materials' interface in selective hydrogenation of CO₂ to CH₃OH, Angew. Chem. Int. Ed. 50 (2011) 2162–2165.

[45] M.G. Sanchez, J.L. Gazquez, Oxygen vacancy model in strong metal-support

[46] J.C. Frost, Junction effect interactions in methanol synthesis catalysts, Nature 334 (1988) 577–580.

[47] K.M. Neyman, K.H. Lim, Z.-X. Chen, L.V. Moskaleva, A. Bayer, A. Reindl, D. Borgmann, R. Denecke, H.-P. Steinrueck, N. Roesch, Microscopic models of PdZn alloy catalysts: structure and reactivity in methanol decomposition, Phys. Chem. Chem. Phys. 9 (2007) 3470–3482.

[48] A. Karim, T. Conant, A. Datye, The role of PdZn alloy formation and particle size on the selectivity for steam reforming of methanol, J. Catal. 243 (2006) 420–427.

[49] W. Stadlmayr, S. Penner, B. Kloetzer, N. Memmel, Growth, thermal stability and structure of ultrathin Zn-layers on Pd(111), Surf. Sci. 603 (2009) 251–255.

[50] J.A. Lipton-Duffin, J.M. MacLeod, M. Vondracek, K.C. Prince, R. Rosei, F. Rosei, Thermal evolution of the submonolayer near-surface alloy of ZnPd on Pd(111), Phys. Chem. Chem. Phys. 16 (2014) 4764–4770.

[51] T. Conant, A.M. Karim, V. Lebarbier, Y. Wang, F. Girgsdies, R. Schloegl, A. Datye, Stability of bimetallic Pd-Zn catalysts for the steam reforming of methanol, J. Catal. 257 (2008) 64–70.

[52] J.A. Rodriguez, Interactions in bimetallic bonding: electronic and chemical properties of PdZn surfaces, J. Phys. Chem. 98 (1994) 5758–5764.

[53] E. Jeroro, V. Lebarbler, A. Datye, Y. Wang, J.M. Vohs, Interaction of CO with surface PdZn alloys, Surf. Sci. 601 (2007) 5546–5554.

[54] Y. Cao, Z. Sui, Y. Zhu, X. Zhou, D. Chen, Selective hydrogenation of acetylene over Pd-In/Al₂O₃ catalyst: promotional effect of indium and composition-dependent performance, ACS Catal. 7 (2017) 7835–7846.

[55] P.S. Wehner, G.C. Tustin, B.L. Gustafson, XPS study of the reduction and reoxidation of ZnO-supported palladium, J. Catal. 88 (1984) 246–248.

[56] E. Castillejos-Lopez, G. Agostini, M. Di Michel, A. Iglesias-Juez, B. Bachiller-Baeza, Synergy of contact between ZnO surface planes and PdZn nanostructures: morphology and chemical property effects in the intermetallic sites for selective 1,3-butadiene hydrogenation, ACS Catal. 7 (2017) 796–811.

[57] M.D. Morse, Clusters of transition-metal atoms, Chem. Rev. 86 (1986) 1049–1109.

[58] M. Samadi, H.A. Shivaee, A. Pourjavadi, A.Z. Moshfegh, Synergism of oxygen vacancy and carbonaceous species on enhanced photocatalytic activity of electrospun ZnO-carbon nanofibers: charge carrier scavengers mechanism, Appl. Catal. A-Gen. 466 (2013) 153–160.

[59] X.-G. Han, H.-Z. He, Q. Kuang, X. Zhou, X.-H. Zhang, T. Xu, Z.-X. Xie, L.-S. Zheng, Controlling morphologies and tuning the related properties of nano/micro-structured ZnO crystallites, J. Phys. Chem. C. 113 (2009) 584–589.

[60] G.H. Graaf, P. Sijtsema, E.J. Stamhuis, G.E.H. Joosten, Chemical equilibria in methanol synthesis, Chem. Eng. Sci. 41 (1986) 2883–2890.

[61] H.D.B. Jenkins, Le Chatelier's principle, Chemical Thermodynamics at a Glance, Blackwell Publishing Ltd, Oxford, UK, 2008, pp. 160–163.

[62] D. Ehrlich, S. Wohlrab, J. Wambach, H. Kuhlenbeck, H.J. Freund, Reaction of CO₂ on Pd(111) activated via promotor action of alkali coadsorption, Vacuum 41 (1990) 157–160.

[63] J. Saussey, J.C. Lavalley, C. Bovet, Infrared study of CO₂ adsorption on ZnO adsorption sites, J. Chem. Soc., Faraday Trans. I. 78 (1982) 1457–1463.

[64] J. Kossmann, G. Rossmueller, C. Haettig, Prediction of vibrational frequencies of possible intermediates and side products of the methanol synthesis on ZnO(000ī) by ab initio calculations, J. Phys. Chem. 136 (2012).

[65] M. Bowker, H. Houghton, K.C. Waugh, Mechanism and kinetics of methanol synthesis on zinc oxide, J. Chem. Soc. Faraday Trans. I 77 (1981) 3023–3036.

[66] X. Zhou, J. Qu, F. Xu, J. Hu, J.S. Foord, Z. Zeng, X. Hong, S.C.E. Tsang, Shape selective plate-form Ga₂O₃ with strong metal-support interaction to overlying Pd for hydrogenation of CO₂ to CH₃OH, Chem. Comm. 49 (2013) 1747–1749.

[67] Q.-L. Tang, Q.-H. Luo, Adsorption of CO₂ at ZnO: a surface structure effect from DFT+U calculations, J. Phys. Chem. C 117 (2013) 22954–22966.